COBEM 2023 27TH INTERNATIONAL CONGRESS OF MECHANICAL ENGENEERING

ABCM Brazilian Society of Mechanical Sciences and Engineering
27th ABCM International Congress of Mechanical Engineering
December 04-08, 2023, Florianópolis-SC, Brazil

COB-2023-1111
EFFECT OF HELICAL GEOMETRY ON FLOW/PRESSURE FLUCTUATION ATTENUATOR DEVICE FOR PULSED FLOWS

Matheus Campos Vieira
Gustavo Cordeiro Barreiro
Pedro Henrique Bergamim Bis
João Paulo Barbosa
Ayrton Cavallini Zotelle
Renato do Nascimento Siqueira
LPMF, Department of Mechanical Engineering, Instituto Federal do Espírito Santo - campus São Mateus, Rod. BR 101 norte, km 58, Litorâneo, São Mateus, ES, 29932-540, Brazil
matheuscamposvieira@hotmail.com
guicordeiro42@gmail.com
pedrobbis@hotmail.com
jpbarbosa@ifes.edu.br
ayrton.zotelle@ifes.edu.br
renatons@ifes.edu.br

Abstract. *A solution to minimize oscillations caused by the use of positive displacement pumps is the use of flow/pressure attenuators, also known as flow attenuators. In-line models are widely used due to their geometric characteristics, not depending on gases, suffering less interference from thermodynamic factors, which makes them more efficient in a wide range of operating conditions. The article aims to investigate more efficient attenuator geometries, in particular the helical tubular configuration, in order to minimize pressure and flow oscillations. To evaluate the influence of the parameters, numerical simulations were performed with the Ansys 2023R1 package and the Fluid-Structure Interaction (FSI) approach. The research started from the analysis of two distinct geometries, the attenuators were considered Mooney-rivlin hyperelastic material and the fluid water in laminar regime. The results indicated that the helical configuration presented a flow attenuation of* 6.7% *and a peak pressure reduction of* 9.6%*, while the reference geometry presented a flow attenuation of* 11.3% *and a pressure reduction of* 7.3%*. The analysis of the differences between the geometries revealed that the helical configuration has greater efficiency for energy dissipation, due to its curvature, which contributed to a decrease in pressure peaks.*

Keywords: *Flow Damper, Accumulator, Fluid-Structure Interaction, Hyperelastic Materials, Helical Attenuator.*

1. INTRODUCTION

Positive displacement pumps are widely used in industry due to their high capacity to pump high viscosity fluids. Due to its alternative movement, a pulsed flow appears in the pipe, which forms a complex acoustic system, with many natural, acoustic and mechanical frequencies, being a potential cause of high vibration problems and/or component failure (Wachel and Price, 1988).

Flow pulsation causes a pressure pulsation when there is net resistance in the system. The pressure that propagates through the pipeline can cause vibration, noise, damage, and even rupture of the pipeline, in addition to serious safety accidents. The effects of pulsed pressure on hydraulic systems are varied. It affects the service life of hydraulic components, decreases the working accuracy of actuators, affects instrument measurement and increases maintenance expenses. Many hydraulic components are damaged by pressure pulsation. Furthermore, as pointed out by Wang *et al.* (2021b), the pressure oscillation in aircraft hydraulic pipes produces a noise that interferes with the emotions of the crew and passengers, and can cause damage to human health. The same can be applied to industrial lines. Therefore, it is important to control the pressure pulsation in the hydraulic system to avoid such problems.

Pulsation dampers (also known as attenuators) are designed to minimize the effects of pulsation and are used to reduce (Koegler *et al.*, 2017) pressure pulses. Its operating principle is due to the structure's ability to deform, due to the forces of internal pressure, and to store fluid inside, which will then be supplied again to the system. Its deformable structure varies with the type of attenuator.

Some factors directly interfere with the efficiency of the attenuators, such as the deformable material and its geometry. Elastomers are widely used in attenuators because elastomers are polymers that, at room temperature, can be repeatedly

deformed to at least twice their original length. In addition, when the effort is removed, it should quickly return to its original dimensions. Another factor is the constructive geometry of the attenuator, as described. There are several models currently available, which can be influenced by the complexity of its internal geometry, the increase in pressure drop and the deformable element (Canevarolo, 2006).

The industry is constantly evolving, aiming to reduce the cost of production. For this, it is necessary to reduce maintenance expenses and stoppages, in addition to increasing the efficiency of the process. The use of attenuators aims to meet part of these needs. Therefore, it is necessary to analyze the proposal of new geometries, such as the helical format, to obtain satisfactory results.

The proposed geometry suggests a product with a shorter length along the pipeline and attenuation greater than or equivalent to the attenuators in a horizontal line. The study used numerical tools and Fluid-Structure Interaction analyzes to confirm these statements, with the aim of analyzing its behavior in more depth.

2. METHODOLOGY

This research is an investigation of the events that occur in the attenuators, using a numerical approach. For this purpose, a computational modeling of the problem was carried out, using the Fluid Structure Interaction approach. Modeling was performed using ANSYS System Coupling® software for two-way coupling. FLUENT® software for calculating Computational Fluid Dynamics, using the Finite Volume Method and Mechanical® for calculating structural deformation, using the Finite Element Method.

The purpose of the study is to analyze the helical geometry for the resistive in-line attenuator. For this, it is essential to improve and adjust the studied geometry to establish comparison parameters. To compare, in all geometries, an internal diameter of 12.7 mm and a thickness of 1 mm were adopted in the attenuator models, which are usual values in the industry.

The straight reference (AR) standard geometry is the first to be worked on, being the efficiency comparison parameter. The length is 600 mm, according to commercial values. To reduce the computational cost, a fraction of 1/4 of the section was used, with the condition of symmetry in the other planes, as indicated in Fig. 1a.

The next step is to analyze the helical geometry (AH), observed in Fig. 1b, to compare the total length of the attenuator of 600 mm, arranged in an arc shape, with helical radius of curvature 95.5 mm. In addition, another relevant variable is the horizontal displacement caused by the revolution of the material, the distance between sections, adopted as 14.7 mm, aiming at the smallest displacement.

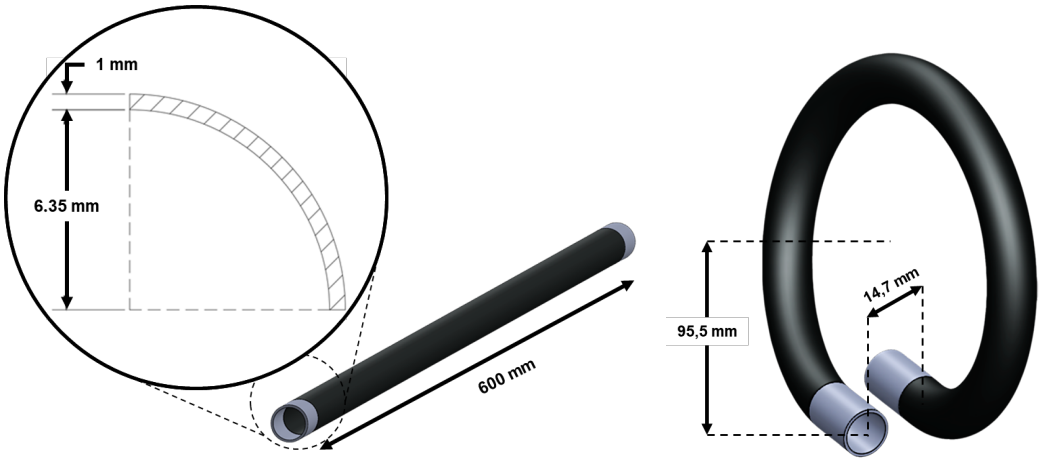

(a) (b)

Figure 1: Dimensions of the geometries of the attenuators used.

After defining the geometries, the working conditions for the simulation were established, such as the parameters adopted in the structural and fluid dynamic domains, as well as the coupling. The boundary conditions of the fluid dynamic domain were initially considered steady state, aiming at the complete filling of the fluid inside the attenuator, minimizing coupling problems. Furthermore, the flow was modeled as incompressible, Newtonian and laminar. The working fluid used was water, with density $\rho = 998\ kg/m^3$ and dynamic viscosity $\mu = 1.003 \times 10^{-3}\ Pa.s$. The outlet boundary was relative pressure $0\ Pa$ and non-slip condition on the pipe walls.

To represent the flow generated by a positive displacement pump, the sinusoidal velocity was used as an input condition, according to Eq. 1. An induced head loss of $2\ kPa$ was also considered, representing the adjacent hydraulic components.

$$U_e(t) = 0.0949 + 0.0474 \cdot \pi \cdot t. \tag{1}$$

Regarding the structure, the attenuator material was considered, natural rubber, a material widely used in elastic hoses. The hyperelastic computational method used in this domain was the two-parameter Mooney-Rivlin model, which uses the properties of natural rubber extracted from the Shahzad *et al.* (2015) article, according to the values declared in the Table 1. In addition, fixed support at the end of the tube and the internal face of the attenuator were considered as information transfer areas with System Coupling®.

Table 1: Mooney-Rivlin method coefficients for natural rubber.

Variable	**Value**	**Unit**
Density	1.21	g/cm^3
C_{10}	0.3339	MPa
C_{01}	$-3.37 \cdot 10^{-4}$	MPa
D_1	$1.5828 \cdot 10^{-3}$	-

adapted fromShahzad *et al.* (2015)

In the coupling, fluid dynamic pressure changes and structural deformations with two-way transient Fluid-Structure analysis (two-way FSI) were used. The total simulation time is 4 seconds, with a time step of 0.1 seconds, with a minimum rate of iterations per time step of 5 and a maximum of 20. With 4 periods of oscillations, the wave becomes cyclic, where the difference between the amplitudes is not considerable.

To validate the numerical model presented, a simulation of the same case presented by Klas and Fialová (2019) was carried out, comparing the data obtained with the results presented. In the paper, only the experimental results and the one-dimensional FSI simulation model of a flexible pipe with the Mooney-Rivlin solid were considered valid.

3. MATHEMATICAL FORMULATION

3.1 Structural governing equations

For a more complete understanding of the numerical study, it is essential to understand the governing equations for the elastic tube, which are presented below. Equation 2 is the Cauchy stress and Eq. 3 is the moment equation.

$$\overline{\overline{\sigma}} = -p\overline{\overline{\delta}} + \left[\left[2\frac{\partial W}{\partial I_1}\overline{\overline{b}} - 2I_3\frac{\partial W}{\partial I_2}\overline{\overline{b}}^{-1}\right]\right]. \tag{2}$$

Equation 2 describes the stress tensor in terms of invariants, used in constitutive models of hyperelastic materials (Hos, 2009). The first term represents the isotropic contribution of the hydrostatic pressure, where p is the pressure field and $\overline{\overline{\delta}}$ is the Kronecker delta. The second term of the equation represents the contribution due to stresses, which W is the strain energy function. For the study, modeling by the Mooney-rivlin method is necessary. I_1, I_2 and I_3 are the invariants of the strain tensor, and $\overline{\overline{b}}$ the strain tensor (ANSYS, 2023). With the tension, it is possible to obtain the displacement through the equation of moment.

$$\rho_s\ddot{\vec{d}} = \nabla \cdot \overline{\overline{\sigma}} + \vec{f_s}. \tag{3}$$

Equation 3 describes the moment in the structure (Akbar, 2022; Sang *et al.*, 2017). This equation relates the second-order time derivative of deformation ($\ddot{\vec{d}}$) with the stresses applied to the structure, being the sum of the Cauchy stress, Eq. 2, resulting from the deformation of the element, and external forces, in $\vec{f_s}$, including the forces caused by the fluid in the FSI. The term ρ_s, represents solid density.

3.2 Governing equations for the fluid

For the equation of the fluid, an incompressible and Newtonian fluid was considered. This consideration simplifies the continuity equation for a deforming control volume to be Eq. 4.

$$\frac{\partial \rho_f}{\partial t} + \nabla \cdot (\rho_f \vec{U}) + \frac{1}{V_m}\left[\frac{\partial}{\partial t}\int_{Vc} \rho_f \, dV(t) + \int_{Sc} \rho_f \vec{U} \cdot \vec{n} \, dA(t)\right] = 0, \tag{4}$$

where ρ_f is the density of the fluid, t the time, $\vec{U}$ the velocity vector, V_m the average volume of the fluid in the control volume and $\vec{n}$ the normal vector to the surface. The momentum equation for the variable control volume is presented in Eq. 5.

$$\rho_f \frac{\partial(\vec{U})}{\partial t} + \rho_f \vec{U} \cdot (\nabla \vec{U}) = -\nabla p + \mu(\nabla^2 \vec{U}) + \vec{f_f}, \tag{5}$$

where ρ_f, μ, p are the fluid density, dynamic viscosity, pressure field, respectively. The external forces per unit volume applied to the fluid, which come from the structural, are represented by the term $\vec{f_f}$. The current equation considered constant density and viscosity and laminar flow. The first part of the equation presents the rate of change of the fluid momentum, while the second part describes the influence of pressure, viscosity and external forces on the fluid velocity (Akbar, 2022; Sang *et al.*, 2017; Tey *et al.*, 2017).

3.3 Governing equations at the fluid-solid interface

In Fluid-Structure Interaction, the coupling relationship procedure is described according to Axisa and Antunes (2007) as the structure modifying the flow conditions at the fluid interface, which, in turn, induces fluctuations in pressure and/or viscous forces; the load applied to the fluid-structure interface subsequently alters the motion of the structure. This cycle repeats with each interaction, due to the dependency on the current state. To achieve this, two conditions must be met at the fluid-structure interface, as mentioned by (Akbar, 2022). The first condition, expressed in Eq. 6, ensures geometric compatibility.

$$d_f = d_s, \tag{6}$$

where d_f and d_s are the displacement of the fluid and solid elements at the contact interface, respectively. To ensure that there are no empty areas between them, it is necessary that the meshes are compatible. The second condition establishes the traction balance:

$$\vec{\sigma}_f \cdot \vec{n}_f + \vec{\sigma}_s \cdot \vec{n}_s = 0, \tag{7}$$

$\vec{\sigma}_f$ and $\vec{\sigma}_s$ are fluid and solid stress vectors, and $\vec{n}$ is the unit vector normal to the interface.

These governing equations at the fluid-solid interface are essential to ensure the integrity and physical coherence of the coupling between the two domains, enabling a precise analysis of the behavior of the FSI (Akbar, 2022) system.

4. RESULTS AND DISCUSSION

To analyze the results, it is important to point out that the numerical results are still influenced by errors caused by residuals, due to initial values. As interactions and simulation time increase, these differences tend to decrease, presenting more reliable results. To avoid this type of problem, the graphics had a minimum time of $1\ s$ to be seen (equivalent to 1 cycle). For purposes of calculating the attenuation and equations of the curves, an analysis time interval between 3 and 4 seconds was established, where the curve has already become cyclic.

4.1 Secondary flow in helical attenuators

Another important point to be studied when working with flow in curved tubes is the emergence of secondary flow. Given the initial conditions of the flow and the geometry of the attenuator, the Dean Number was calculated, thus, an average Dean Number of, $De_m = 309$ was obtained. This value indicates the existence of a secondary flow, as demonstrated by Nivedita *et al.* (2017). Observing Fig. 2, one can see the velocity distribution in three different positions along the tube, and three different input velocities.

In the first column, it is possible to notice that the entry velocity is developed, as established in the boundary conditions. In the second column, located in the middle section along its length, the emergence of secondary flow is already observed. Given that the Dean vortices appear before half the length of the tube, this suggests that changing the flow has an impact on the attenuation. In the third column, it is possible to notice that the flow pattern did not change significantly from the middle of its length, demonstrating that, for the same instant of time, the adopted frequency presented only one pulse of the entry velocity along its length.

In Fig. 2, the lines represent the maximum, intermediate and minimum values, respectively, for the time interval between 3 and 4 seconds. It is observed, when analyzing the lines, that the fluid presents stagnation zones in the upper part of the tube with the passage of time. This phenomenon is caused by centripetal and centrifugal forces, which results in a higher velocity on the outer wall of the curvature. The understanding of this phenomenon is of great importance, since the differentiation between the geometries is due to the appearance of this phenomenon.

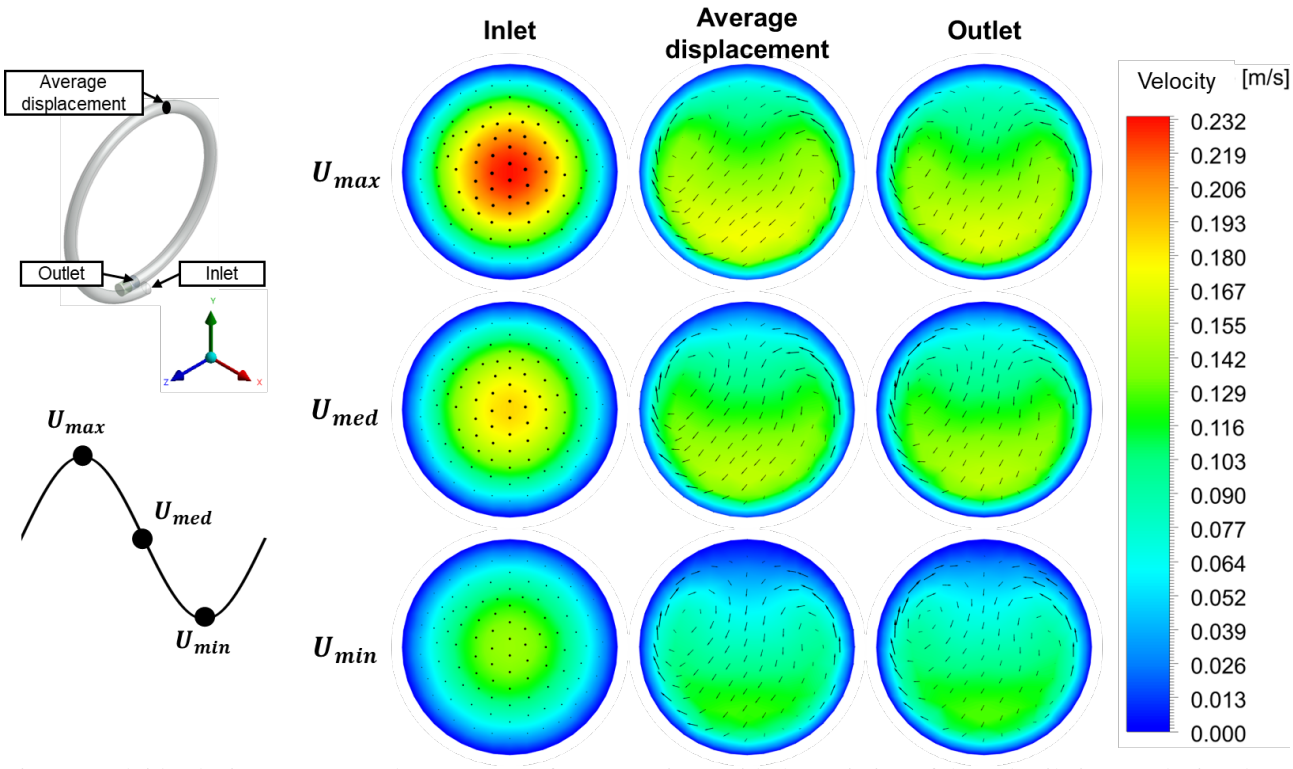

Figure 2: Fluid velocity contours and appearance of Dean vortices, with the variation of the pulsatile input velocity along the length of the helical attenuator.

4.2 Comparison of speeds in different geometries

The FSI assessment enables analysis of both structural and fluid dynamics. Initially, the evaluation of the fluid dynamics was divided to evaluate the flow decrease and the pressure decrease. The flow was verified considering the velocity parameters for the inlet and outlet section, without changing the area.

Observing Fig. 3, where it compares the output speeds of the models with the input, it is possible to notice a decrease in speed in both cases and also a difference between the models. It is possible to determine these differences by comparing the equations of the curves, Eq. 1, 8 and 9.

With the Origin® software in its student version, it was feasible to determine the equation for the output velocity of the rectilinear attenuator, Eq. 8, with an adjustment coefficient of $R^2 = 0.99999$.

$$U_{o_R}(t) = 0.096 + 0.021 \cdot (2 \cdot \pi \cdot 0.99971 \cdot (t - 0.052)) \,. \tag{8}$$

In the same way, Eq. 9 was determined for the output speed for the helical attenuator, with an adjustment coefficient of $R^2 = 0.99991$.

$$U_{o_H}(t) = 0.096 + 0.022 \cdot (2 \cdot \pi \cdot 0.99898 \cdot (t - 0.039)) \,. \tag{9}$$

Comparing the Equations 8 and 9, the difference between the geometries is evident. In both equations in relation to the input velocity, Eq. 1, it is noted that the average velocity showed an increase of approximately 1%, which makes the amplitude even smaller, resulting in greater attenuation. The average speed showed an increase due to mistakes made by the numerical analysis, such as the mesh. When comparing the frequencies, in both cases they were approximately equal, as observed in Wang *et al.* (2021b)'s work for resistive attenuators, in which this type of model does not change the system frequency.

It is also possible to check the flow attenuation of each device. Where the parameter represents the level of absorption between the amplitudes of the incoming and outgoing waves, being calculated as:

$$\%A = \left(1 - \frac{Y_f(t) - Y_m}{Y_i(t) - Y_m}\right) \cdot 100. \tag{10}$$

The variable $Y_i(t)$ represents the value of the property at the input, the $Y_f(t)$ at the output and Y_m the average value, being the most important variable in question in this work. This calculation is the result of simplifying the equation proposed by Santos *et al.* (2021).

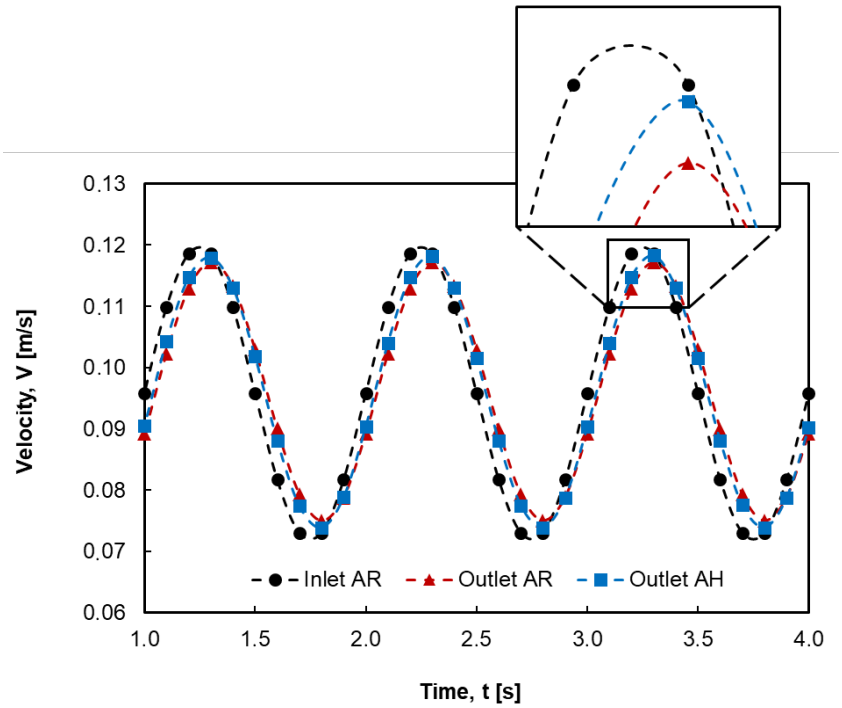

Figure 3: Comparison of input and output speeds for the two configurations.

The rectilinear model presented a flux attenuation of approximately 11.3%, while the helical model of 6.7%. Despite being similar, the helical attenuator had a lower attenuation in the flow in relation to the straight one, due to the curvature affecting the velocity along the tube. The helical attenuator has higher velocity on the outside of the bend, which is not good for deformable material as its stresses are not evenly distributed along the circumference of the tube. Therefore, this consideration becomes crucial when sizing attenuators for applications that require a specific level of attenuation.

4.3 Comparison of pressures in different geometries

Another relevant factor to be evaluated is whether there was a decrease in pressure peaks. When analyzing the pressures in the attenuators, there is a significant difference in the attenuation of the pressure peaks between the helical and rectilinear configurations. Fig. 4 clearly illustrates this discrepancy, showing that the maximum pressure at the helical attenuator output is higher compared to the rectilinear attenuator output.

The comparison between the models is evidenced by the pressure equations, following the same velocity procedures. The inlet pressure, however, was not established initially, being acquired after the simulations, obtaining the Eq. 11 for the rectilinear attenuator, with an adjustment coefficient of $R^2 = 0.99993$.

$$P_{i_R} = 1628 + 385 \cdot (2 \cdot \pi \cdot 1 \cdot (t - 8.017)) \,. \tag{11}$$

For the output pressure curve for the rectilinear configuration, the Eq. 12 was obtained, with a precision of $R^2 = 1$.

$$P_{o_R} = 1615 + 357 \cdot (2 \cdot \pi \cdot 0.99947 \cdot (t - 9.054)) \,. \tag{12}$$

The helical model presented the Eq. 13 for the inlet pressure curve, with an adjustment coefficient of $R^2 = 0.9984$.

$$P_{i_H}(t) = 1644 + 417 \cdot (2 \cdot \pi \cdot 1 \cdot (t - 2.004)) \,. \tag{13}$$

And for the output, the Eq. 14 was obtained, with a precision of $R^2 = 0.99992$.

$$P_{o_H}(t) = 1615 + 377 \cdot (2 \cdot \pi \cdot 0.99906 \cdot (t - 2.038)) \,. \tag{14}$$

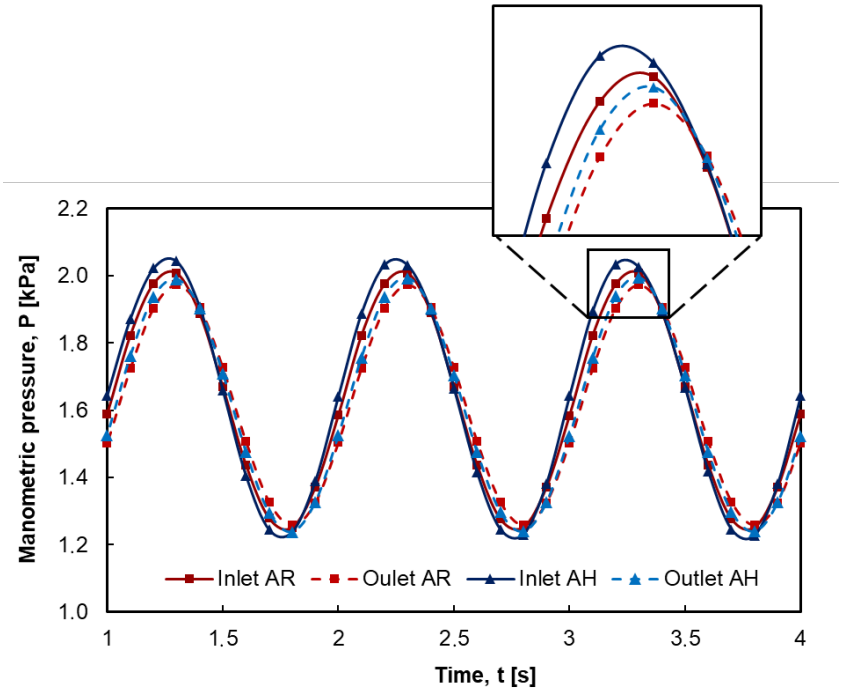

Figure 4: Comparison of inlet and outlet pressures for the two configurations.

When analyzing the equations, it is possible to notice a reduction of the average pressure in both configurations of approximately 1%. Furthermore, the frequencies were approximately equal, as evidenced in the literature. The pressure attenuation was different between the models, with an attenuation of 7.3% for the rectilinear attenuator, and 9.6% for the helical attenuator. This difference is attributed to the peculiar geometry of the helical configuration, which promotes greater flow redirection and distribution.

It is important to note that the input pressure to the helical attenuator is greater than that of the rectilinear attenuator input. This indicates that the flow entering the helical attenuator already has a higher pressure, which can affect the flow behavior and the attenuator deformation. The inlet pressure has a direct impact on the distribution of stresses within the device, affecting its ability to attenuate pressure fluctuations. Therefore, the difference in inlet pressure between the helical and straight configurations contributed to the variation in the attenuation of the pressure peaks.

4.4 Comparison of deformations in different geometries

For the analysis of structural deformation, a position was adopted for the study. The element's position was chosen due to its greater deformation along its length. The element, called midpoint, is located on both attenuators exactly halfway along the length of the tube, at $300\ mm$, and on the outer diameter of the attenuator, as illustrated in Fig. 5.

With the selected point, it was possible to analyze the deformation in the attenuators. As shows Fig. 6, the deformation scales were entirely different. The rectilinear attenuator presents uniform radial deformation along its length, since gravity is not considered in the problem, whereas the helical attenuator presents non-uniform deformation along its length, due to its higher degrees of freedom.

When examining Fig. 6, it is noticed that there is no deformation of the element in the X axis of the rectilinear configuration. The reason for this fact is the position of the study site. The point is located at the origin, in the direction of the X axis, which indicates that the radial deformation will only be in the Y direction. However, this consideration has no impact on the helical attenuator, which, due to its step in the revolution, presents deviations in the X direction.

The analysis on the Y axis in Fig. 6, due to the location of the study points, reveals the variation in the internal volume for the accumulation of liquids, making it possible for the attenuator to fulfil its attenuating function. In this way, both were similar over longer periods of time, since, in the first seconds, the helical geometry was adapting to the movement, starting from rest, presenting a damping of the vibrations, while the deformation of the straight line became cyclic, together with the flow inside it.

Regarding the Z axis in Fig. 6, axial axis, there was also a displacement of the element. Its displacement is counter-intuitive, since the ends of the tube are fixed. Its movement is possible because there is a non-slip condition on the walls that are in contact with the fluid. The friction between the flowing fluid and the wall, combined with the flexibility offered by natural rubber, promotes axial movement.

In relation to the rectilinear one, the displacements in Z were not as expressive as those of the helical attenuator,

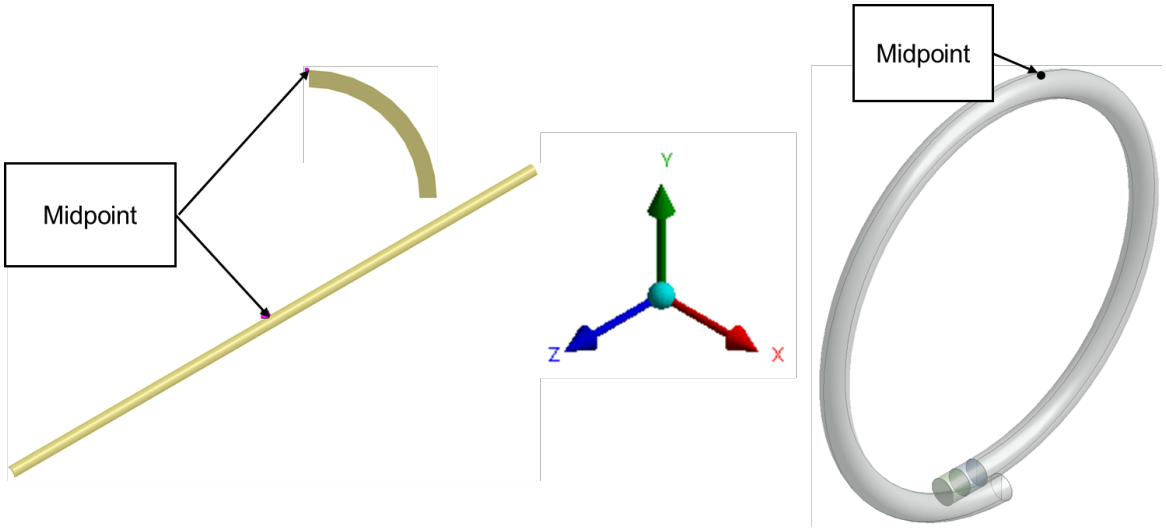

Figure 5: Location of the study point for the structural deformation of the attenuator.

however, there was variation. The helical configuration presents greater axial deformations because the flow presents only the Z component at the inlet, reaching curvature at the first moment, resulting in large deformation. Furthermore, it is possible to notice that the displacements did not become cyclical with the simulated time. But it is noticed that there is a convergence regarding the shape of the wave. However, it is expected that there will be more simulation time to achieve this convergence.

It is observed in Fig. 6, that the helical configuration presented greater deformations in all directions, which is related to the degrees of freedom it presents. The attenuator is attached to the ends only, allowing your body to move in all directions. To avoid such movements, in applications such as flocculation, an internal cylindrical surface is used, where the rubber tube is wound, serving as a support. Therefore, the analysis of the displacements of the structural elements is crucial for choosing the material to be used, which results in a major change in the efficiency of the device.

4.5 Shear stresses and velocity and pressure lag in models

Table 2 lists the previously discussed values for easy comparison. Observing the table, it is noticed that the rectilinear configuration presented a greater flow attenuation, and consequently a greater lag between the inlet and outlet curves. The helical attenuator, on the other hand, presented a significant reduction in pressure, attributed to the curvature of the geometry, which may have caused the appearance of the secondary flow, which, in turn, requires energy in the form of pressure, such as ignition. The pressure lag is important, as both geometries were the same. This aspect is not related to the geometry itself. The lag is related to the flow distribution and the shear stresses on the vessel wall (Wang *et al.*, 2021a).

Table 2: Attenuation and lag variables for pressure and flow from the attenuator settings.

Variables	Rectilinear configuration	Helical configuration
Flow attenuation, $\%A_Q$	11.3%	6.7%
Flow lag, ω_Q	$18.8°$	$13.9°$
Pressure attenuation, $\%A_P$	7.3%	9.6%
Pressure lag, ω_P	$11.4°$	$11.4°$

To understand the phenomena in question, it is important to verify the shear stress distributions along the length of the tube. By examining Fig. 7, where the stress distribution is shown in the rectilinear attenuator during a time interval equal to $3.3\ s$, which represents the most intense stress on the structure, it is possible to notice that the shear stress far from the edge remains constant. Having a maximum value of $15,216\ kPa$ in its interior. This information is crucial to the discussion of attenuator offset angle.

Similarly, when examining Fig. 8, where the stress distribution is shown during the same interval, it is possible to notice that the shear stresses along its geometry are not uniform, with locations in its interior having a maximum value of $15.714\ kPa$.

Therefore, when analyzing Figures 7 and 8, it can be seen that the shear stresses behave differently in each geometry. In the rectilinear attenuator, the voltage distribution is uniform and constant inside it. In the helical, the stresses vary along the geometry, being punctual. Wang *et al.* (2021a) in his research, demonstrates that the lag in slightly curved

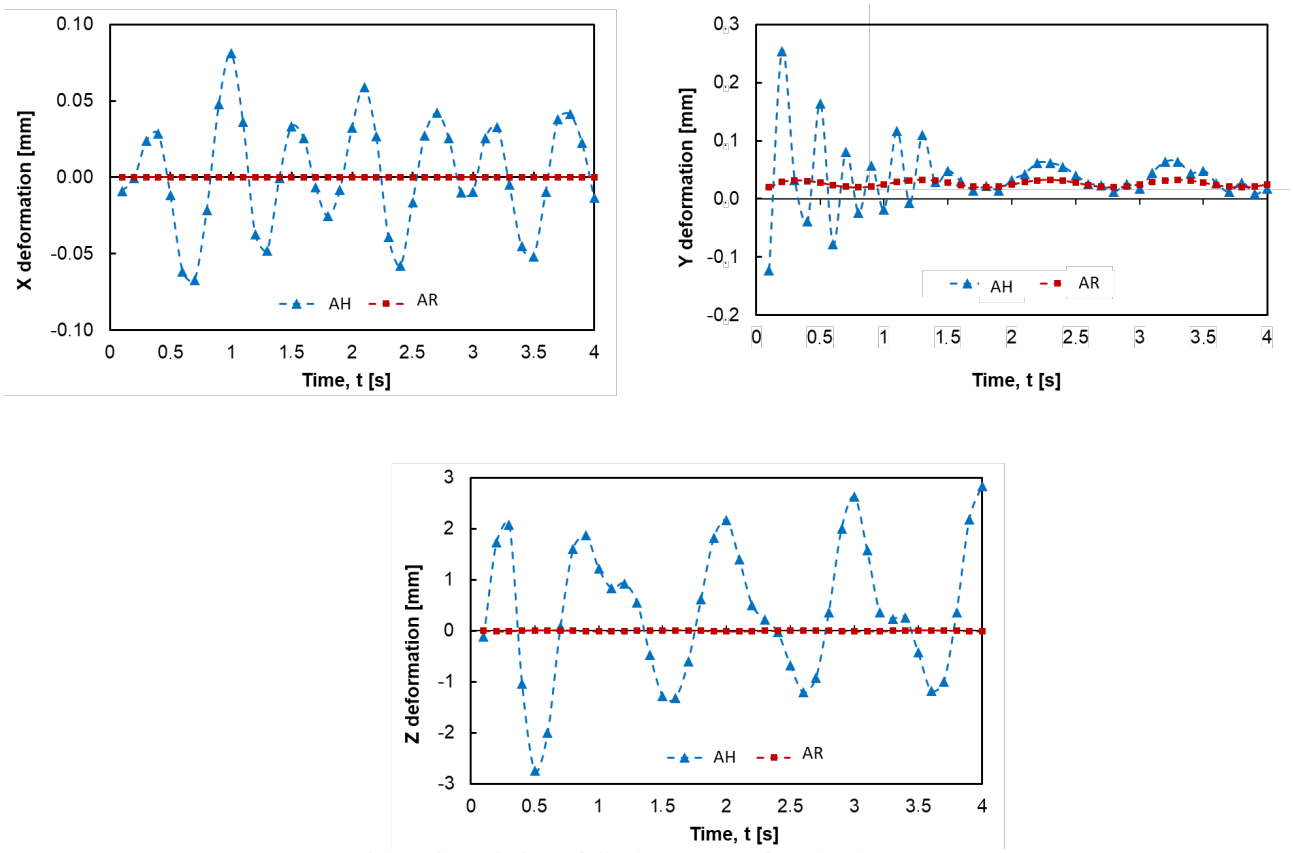

Figure 6: Variation of displacements of study elements.

Figure 7: Analysis of the shear stress at the instant of 3.3 s, in the straight attenuator.

tubes varies punctually with the stresses, which results in a smaller final lag. Justifying different lag values between the studied models. Since the lag is related to the flow distribution, the lag occurs only in the flow graph, without affecting the pressure, as you can see in Table 2.

5. CONCLUSION

The results of the numerical simulations of the two-way fluid-structure interaction allowed the analysis of the behavior of the resistive attenuators, demonstrating that the helical configuration and the straight reference geometry can attenuate the flow and reduce the pressure peaks. The helical configuration had a flow reduction of 6.7% compared to the reference geometry, which had a flow reduction of 11.3%. Regarding the reduction of pressure peaks, the helical attenuator was more efficient, with a significant decrease of 13.9%, compared to the reduction of 7.3% observed in the rectilinear configuration. These results indicate that the helical configuration has the potential to improve the performance of pressure attenuators. The helical configuration suffered more deformation due to the number of additional degrees of freedom relative to the reference geometry. The proposed configurations presented consistent results. However, it is essential to carry out additional experiments to validate numerical results and ensure their practical applicability. The results demonstrate the relevance of the design in analysis of non-conventional geometries, such as curved attenuators, to optimize the attenuators' performance. These findings provide a basis for further research and development of more efficient attenuators suited to the specific needs of different industrial and biomedical applications.

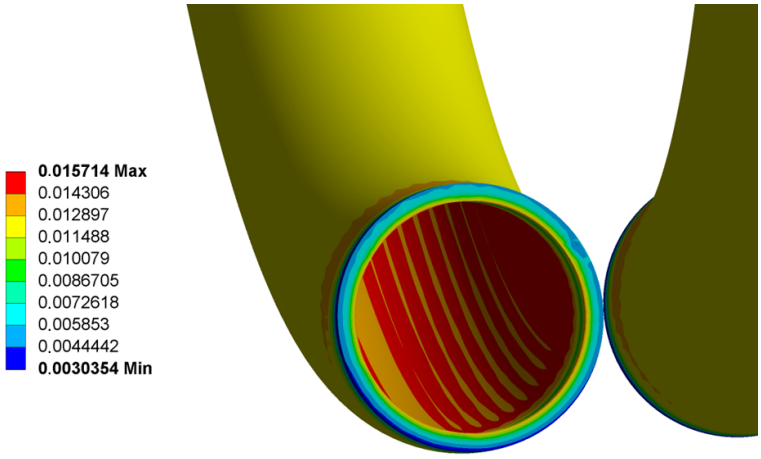

Figure 8: Analysis of the shear stress at the instant of 3.3 s, in the helical attenuator.

6. REFERENCES

Akbar, B., 2022. *Mathematical Modelling and Simulation of Flow in Collapsible Tubes*. Mestrado em engenharia mecânica, Norwegian University of Science and Technology.

ANSYS, 2023. *Theory Reference*. ANSYS, Inc., Pensilvânia, EUA.

Axisa, F. and Antunes, J., 2007. *Modelling of mechanical systems*, Vol. 3. Elsevier Ltd., Great Britain, 1st edition. ISBN 978-0-750-66847-7.

Canevarolo, S.V.J., 2006. *Ciência dos polímeros*. Artliber Editora Ltda., São Paulo, 2nd edition.

Hos, L., 2009. *Modelos constitutivos hiperelásticos para elastômeros incompressíveis*. Mestrado em engenharia mecânica, Universidade Federal do Rio Grande do Sul, Porto Alegre.

Klas, R. and Fialová, S., 2019. "Pulse flow of liquid in flexible tube". *EPJ Web Conf.*, Vol. 213, p. 02041. doi: 10.1051/epjconf/201921302041.

Koegler, A.F., Haselmann, D., Alt, N.S.A. and Schluecker, E., 2017. "Experimental characterization of a flow-through pulsation damper regarding pressure pulsations and vibrations". *Chemical Engineering Technology*, Vol. 40, No. 1, pp. 162–169. doi:10.1002/ceat.201600175.

Nivedita, N., Ligrani, P. and Papautsky, I., 2017. "Dean flow dynamics in low-aspect ratio spiral microchannels". Vol. 7, No. 1, p. 44072. ISSN 2045-2322. doi:10.1038/srep44072.

Sang, h., Ngo, L., Muhammad, S., Jeon, B. and Choi, H., 2017. "A comparative study between partitioned and monolithic methods for the problems with 3d fluid-structure interaction of blood vessels". *Journal of Mechanical Science and Technology*, Vol. 31, pp. 281–287. doi:10.1007/s12206-016-1230-2.

Santos, M.d.O.d., Ribeiro, D.d.C., Barbosa, J.P. and Siqueira, R.d.N., 2021. "A modified windkessel model applied in a tubular pulsation dampener analysis". In *International Congress of Mechanical Engineering*. AssociaÇão Brasileira de Engenharia e Ciências Mecânicas, Brazil, p. 10.

Shahzad, M., Kamran, A., Siddiqui, M.Z. and Farhan, M., 2015. "Mechanical characterization and fe modelling of a hyperelastic material". *Materials Research*, Vol. 18. doi:10.1590/1516-1439.320414.

Tey, W.Y., Asako, Y., Che Sidik, N.A., Che Sidik, N.A., Rui-Zher, G., Malaysia, U. and Lumpur, K., 2017. "Governing equations in computational fluid dynamics: Derivations and a recent review". Vol. 1, pp. 1–19.

Wachel, J. and Price, S., 1988. "Understanding how pulsation accumulators work". *Pipeline Engineering Symposium*, Vol. 14, pp. 23–31.

Wang, H., Krüger, T. and Varnik, F., 2021a. "Geometry and flow properties affect the phase shift between pressure and shear stress waves in blood vessels". *Fluids*, Vol. 6, No. 11, p. 378. ISSN 2311-5521. doi:10.3390/fluids6110378.

Wang, Y., Shen, T., Tan, C., Fu, J. and Guo, S., 2021b. "Research status, critical technologies, and development trends of hydraulic pressure pulsation attenuator". Vol. 34, No. 1, p. 14. ISSN 2192-8258. doi:10.1186/s10033-021-00532-z.

7. RESPONSIBILITY NOTICE

The authors are solely responsible for the printed material included in this paper.